CHEMISTRY
A EUROPEAN JOURNAL

DOI: 10.1002/chem.201000584

Density Functional Calculations of ^{55}Mn, ^{14}N and ^{13}C Electron Paramagnetic Resonance Parameters Support an Energetically Feasible Model System for the S_2 State of the Oxygen-Evolving Complex of Photosystem II

Sandra Schinzel,[a, b] Johannes Schraut,[a] Alexei V. Arbuznikov,[a] Per E. M. Siegbahn,[b] and Martin Kaupp*[a]

Dedicated to Professor Paul von Ragué Schleyer on the occasion of his 80th birthday

Abstract: Metal and ligand hyperfine couplings of a previously suggested, energetically feasible Mn_4Ca model cluster (**SG2009^{-1}**) for the S_2 state of the oxygen-evolving complex (OEC) of photosystem II (PSII) have been studied by broken-symmetry density functional methods and compared with other suggested structural and spectroscopic models. This was carried out explicitly for different spin-coupling patterns of the $S=^1/_2$ ground state of the $Mn^{III}(Mn^{IV})_3$ cluster. By applying spin-projection techniques and a scaling of the manganese hyperfine couplings, computation of the hyperfine and nuclear quadrupole coupling parameters allows a direct evaluation of the proposed models in comparison with data obtained from the simulation of EPR, ENDOR, and ESEEM spectra. The computation of ^{55}Mn hyperfine couplings (HFCs) for **SG2009^{-1}** gives excellent agreement with experiment. However, at the current level of spin projection, the ^{55}Mn HFCs do not appear sufficiently accurate to distinguish between different structural models. Yet, of all the models studied, **SG2009^{-1}** is the only one with the Mn^{III} site at the Mn_C center, which is coordinated by histidine (D1-His332). The computed histidine ^{14}N HFC anisotropy for **SG2009^{-1}** gives much better agreement with ESEEM data than the other models, in which Mn_C is an Mn^{IV} site, thus supporting the validity of the model. The ^{13}C HFCs of various carboxylates have been compared with ^{13}C ENDOR data for PSII preparations with ^{13}C-labelled alanine.

Keywords: cluster compounds · density functional calculations · EPR spectroscopy · photosystem II · structure elucidation

Introduction

Dioxygen powers a substantial part of life on earth. Although the dioxygen produced in plant photosynthesis by photosystem II (PSII) may be viewed as a waste by-product, it contains a significant amount of the chemical energy generated by photosynthesis.[1] The catalyst to which two water molecules are coupled in a four-electron oxidation to yield one molecule of O_2 is known to be a protein-bound tetranuclear manganese complex. This cofactor is often denoted the "oxygen-evolving complex" (OEC). Driven by four successive light excitations of the P_{680} chlorophyll dimer of PSII, four electrons are removed from the OEC, which passes through a cyclic sequence of five oxidation states S_0–S_4 (the Kok cycle) before releasing the oxidation product O_2.[2] The removal of four protons has recently received increased attention[3–6] and an extended mechanism has been suggested.[7,8]

Evidently, the question of how Nature creates oxygen by light-driven catalysis is also of central importance for future renewable energy sources.[1] Not surprisingly, structure, protein environment, and function of the OEC have been the focus of a tremendous amount of research over the past 25 years. The methodologies applied range from biochemical studies through X-ray diffraction,[9–13] X-ray absorption spec-

[a] Dr. S. Schinzel, J. Schraut, Dr. A. V. Arbuznikov, Prof. Dr. M. Kaupp
Institut für Physikalische und Theoretische Chemie
Universität Würzburg
Am Hubland, 97074 Würzburg (Germany)
Fax: (+49) 931-888-7135
E-mail: kaupp@mail.uni-wuerzburg.de

[b] Dr. S. Schinzel, Prof. Dr. P. E. M. Siegbahn
Department of Physics, ALBA NOVA
and Department of Biochemistry and Biophysics
Arrhenius Laboratory
Stockholm University, 10691 Stockholm (Sweden)

Supporting information for this article is available on the WWW under http://dx.doi.org/10.1002/chem.201000584.

troscopy (in particular, EXAFS[6,14]), and infrared and optical spectroscopy[15–17] to electron paramagnetic resonance (EPR[18,19]) spectroscopy. Yet the precise structural arrangement of the manganese and calcium centers, bridging ligands, and protein surroundings of the cluster in the different S states, as well as the underlying electronic structure are known only incompletely. X-ray diffraction studies suffer from limited resolution and from radiation damage in the synchrotron beam (in particular, the photoreduction of the Mn^{III} and Mn^{IV} centers to Mn^{II}).[20–23] EXAFS does not exhibit this problem but on its own provides neither a global picture of the cluster nor of the protein surroundings.[6,14,24,25]

Owing to the paramagnetic nature of the manganese centers, EPR spectroscopy and related techniques like electron-nuclear double resonance (ENDOR) or electron-spin-echo-envelope-modulation (ESEEM) provide additional valuable insights. They allow the investigation of short-lived paramagnetic species (with lifetimes down to below 10^{-6} s) and the spin and oxidation states to be partly determined. The S_2 state is by far the best EPR-characterized state of the Kok cycle.[26–34] It exhibits either the so-called multiline signal at $g=2$, which arises from the $S=^1/_2$ ground state, probably with a $Mn^{III}(Mn^{IV})_3$ distribution of oxidation states, or a broad signal at $g=4.1$, attributable most likely to the $S=^5/_2$ spin state with the same manganese oxidation states. The multiline signal indicates an antiferromagnetically coupled mixed-valence manganese cluster that resembles the multiline signal of synthetic or biological dinuclear $Mn^{III}Mn^{IV}$ complexes.[35–37] Hyperfine coupling constants (HFCs) have been extracted by ^{55}Mn ENDOR spectroscopy and reveal significant contributions from all four manganese ions. A variety of EPR and ENDOR simulations of the multiline signal of different samples are available,[30–32] and these have been used in attempts to extract information about the ground state and its spin-coupling patterns. Multifrequency ESEEM spectroscopy has been used to determine the ^{14}N HFC and nuclear quadrupole coupling (NQC) of a histidine protein residue bound to the manganese cluster.[38,39] Recently, ^{13}C ENDOR data were obtained for S_2 state preparations with ^{13}C-labelled alanine.[40]

EPR, ENDOR, or ESEEM studies should benefit greatly from support by quantum-chemical calculations, which may provide structural information as well as insights into the nature of the ground and excited states of the Kok cycle. Owing to the complicated spin-coupling patterns of the formally $S=^1/_2$ ground spin state of the S_2 state, a fully appropriate quantum-chemical treatment would require sophisticated multiconfigurational wavefunctions that incorporate both dynamic and nondynamic electron correlation effects to a large extent. This is currently out of the question for a system of the complexity of the OEC. A possible alternative is to construct so-called broken-symmetry (BS) states within unrestricted Kohn–Sham density functional theory (DFT) followed by appropriate spin-projection procedures.[41–45] This provides access to hyperfine (and nuclear quadrupole) couplings, which enable the quality of the molecular model complexes for the OEC to be evaluated by direct comparison of the calculations with experimental EPR, ENDOR, and ESEEM data. Very recently, Pantazis et al.[45] studied the exchange coupling constants J and the manganese hyperfine couplings of 12 structural models of the S_2 state of the OEC by BS-DFT. After spin projection, the computed isotropic ^{55}Mn HFCs of several models were broadly in the range of values obtained by different simulations of EPR and ENDOR spectra, which indicates that there is a chance that quantum-chemical methods may eventually indeed be used to validate structural proposals.

Most of the model clusters studied in that work were based on the "twisted-core" topology constructed earlier on consideration of X-ray and EXAFS data: Substantial assumptions were involved in these structural proposals. Two of the models (**11** and **12**) were cluster models introduced by Siegbahn. Recent computational work[46] on these cluster models has demonstrated that they give much lower total energies than others based on QM/MM optimizations or on the EXAFS-based twisted-core structures. For example, in the case of the S_2 state, the most recent cluster model of Siegbahn was computed[46,47] to be lower in energy than the twisted-core models by around 35–65 kcal mol^{-1} (145-265 kJ mol^{-1}). Although the cluster model neglects any constraints on the cluster arrangement by the protein environment, the magnitude of these lower energies is far larger than what can be accounted for by the environment. Furthermore, the most recently suggested cluster model, which is based on a clear mechanistic picture of water oxidation at the OEC, agrees well with the available X-ray diffraction and EXAFS data.[48–50] In this work we focus on the computational evaluation of EPR parameters for models of the S_2 state for a closer comparison of Siegbahn's most recent cluster model with one selected from the twisted-core models (several other models have been studied in somewhat less detail and will be mentioned where appropriate). In particular, we extend the calculations from ^{55}Mn HFCs to histidine ^{14}N and alanine ^{13}C EPR parameters, and we will critically examine the spin-projection procedures needed to extract EPR parameters from BS-DFT calculations. Indeed, careful analysis of spin-coupling patterns can also reveal substantial insights into the assumptions inherent in the spectral interpretations available so far. Interestingly, the computed and experimental ^{14}N HFC anisotropies provide evidence for the histidine being bound to the sole Mn^{III} d^4 center in the S_2 state, as is the case so far only in Siegbahn's cluster model.

Theory: EPR Parameter Calculations for Spin-Coupled Multinuclear Complexes

The theoretical background of the computation of EPR parameters by DFT methods is covered in detail elsewhere.[51–57] Here we summarize only the most relevant points and will then proceed to describe the spin-projection techniques needed for the BS calculations on the multinuclear spin-coupled $Mn^{III}(Mn^{IV})_3$ cluster.

Calculation of hyperfine tensors: The leading nonrelativistic first-order contribution to the isotropic HFCs $A_{iso}(N)$ is the Fermi contact term A^{FC} [Eq. (1)].

$$A_{iso}(N) = A^{FC} = \frac{4\pi}{3}\beta_e\beta_N g_e g_N \langle S_Z\rangle^{-1}\sum_{\mu,\nu} P_{\mu\nu}^{\alpha-\beta}\langle\varphi_\mu|\delta(\mathbf{R}_N)|\varphi_\nu\rangle \quad (1)$$

Here β_e is the Bohr magneton, β_N the nuclear magneton, g_N is the g value of nucleus N, $\langle S_Z\rangle$ is the expectation value of the z component of the total electronic spin, $P_{\mu,\nu}^{\alpha-\beta}$ is the spin density matrix, and the summation runs over all basis set atomic orbitals. The components of the nonrelativistic anisotropic tensor are given by Equation (2) in which $r_N = r - \boldsymbol{R}_N$ ($\boldsymbol{R}_N$ is the position vector of nucleus N). In the rest of this section, we will refer to the metal hyperfine interaction and omit subscript N.

$$A_{ij}^{dip}(N) = \frac{1}{2}\beta_e\beta_N g_e g_N \langle S_Z\rangle^{-1}\sum_{\mu,\nu} P_{\mu\nu}^{\alpha-\beta}\langle\varphi_\mu|\mathbf{r}_N^{-5}(\mathbf{r}_N^2\delta_{ij} - 3\mathbf{r}_{N,i}\mathbf{r}_{N,j})|\varphi_\nu\rangle \quad (2)$$

The second-order perturbation treatment of refs. [58,59] is used to compute spin–orbit (SO) corrections for the HFC tensor (in this work, the corrections are only relevant for the metal HFC). At the coupled-perturbed Kohn–Sham level, the dominant SO correction term arises as a second-order cross term between the one- and two-electron SO Hamiltonian h^{SO} and the perturbed Fock operator F', as given in Equation (3):

$$A_{K,\mu\nu}^{SO-I} = \frac{1}{2}\alpha^4 g_e\gamma_K \frac{1}{2\langle S_Z\rangle}\Big[\sum_k^{occ(\alpha)}\sum_a^{virt(\alpha)} \frac{\langle\psi_k^\alpha|h_u^{SO}|\psi_a^\alpha\rangle\langle\psi_a^\alpha|F_v'|\psi_k^\alpha\rangle}{\varepsilon_k^\alpha - \varepsilon_a^\alpha} - \sum_k^{occ(\beta)}\sum_a^{virt(\beta)} \frac{\langle\psi_k^\beta|h_u^{SO}|\psi_a^\beta\rangle\langle\psi_a^\beta|F_v'|\psi_k^\beta\rangle}{\varepsilon_k^\beta - \varepsilon_a^\beta} \quad (3)$$

in which α is the fine-structure constant, γ_K the gyromagnetic ratio of the nucleus, h^{SO} is explained below, F' is the perturbed Fock operator, with $F'_\nu = (\ell_\nu/r^3) - \frac{2}{\alpha}a_0\sum_{k=1}^{n/2} F'_\nu$, in which (ℓ_ν/r^3) is the paramagnetic nuclear-spin electron-orbit (PSO) operator, K'_ν is a component of the response exchange operator, and a_0 is the weight of HF exchange depending on the specific hybrid functional used (see ref. [60] for a related simultaneous CPKS implementation, and also refs. [58,59] for references to earlier work). ψ^σ and ε^σ are spin-polarized Kohn–Sham orbitals and orbital energies, respectively. GGA or LDA functionals lead to an uncoupled DFT (UDFT) treatment for this second-order term ($a_0 = 0$). The HFC computations for the BS states are the basis for subsequent spin projection, as described further below.

Calculation of nuclear quadrupole coupling tensors: For nuclei with $I > {}^1/_2$, their nonspherical charge distribution interacts with the electric field gradient at the nucleus. This interaction is parametrized by the nuclear quadrupole coupling tensor $\mathbf{Q}$. The latter is traceless and can be expressed by Equation (4) in which the nuclear quadrupole coupling constant e^2q_{zzQ}/h depends on the electric field gradient at the nucleus along the principal z axis and η is the asymmetry parameter defined by Equation (5).

$$\vec{I}\mathbf{Q}\vec{I} = \frac{e^2q_{zz}Q/h}{4I(2I-1)}\{[3I_z^2 - I(I+1)^2] + \eta(I_x^2 - I_y^2)\} \quad (4)$$

$$\eta = \left|\frac{q_{xx} - q_{yy}}{q_{zz}}\right| \quad (5)$$

The NQC parameters involve the total electron density rather than the spin density and are thus expected to be already described well by the BS calculation without spin projection, in contrast to the HFC parameters (see below).

Spin-projection techniques: A system with n paramagnetic ions may be described by the effective spin Hamiltonian given by Equation (6) in which $\vec{S}_i$ is the electronic spin operator of ion i and $\vec{B}$ is the external magnetic field.

$$\hat{H}_{eff} = \sum_{i=1}^n \beta\vec{B}\mathbf{g}_i\vec{S}_i + \sum_{i=1}^n \vec{S}_i\mathbf{a}_i\vec{I}_i + \sum_{i=1}^n \vec{S}_i\mathbf{d}_i\vec{S}_i + \sum_{i=1}^n \vec{I}_i\mathbf{p}_i\vec{I}_i - 2\sum_{i<j}^n J_{ij}\vec{S}_i\vec{S}_j \quad (6)$$

The local HFC tensor $\mathbf{a}_i$ ("site value") parametrizes the interaction of $\vec{S}_i$ with the nuclear spin operator of ion i, $\vec{I}_i$. The local g tensor $\mathbf{g}_i$ of ion i parametrizes the interaction of its electronic spin with the external field $\vec{B}$ and the local tensors $\mathbf{d}_i$ express the zero-field splitting (ZFS) of ion i. Local NQC tensors $\mathbf{p}_i$ interact with the nuclear magnetic moments. Finally, J_{ij} represents the isotropic Heisenberg exchange interaction between the paramagnetic centers i and j. For brevity, we have not included the nuclear Zeeman term and the HFC or NQC terms for ligand nuclei (see below). To be able to relate directly to the experimental spectra for a spin-coupled multinuclear cluster like the OEC, one has to account for the exchange-coupled spin states. This requires a spin-coupled representation using the vector spin-coupling model.[51,61–63] We may thus write the spin Hamiltonian of the OEC in terms of effective, coupled tensors (the NQC has been neglected here) that parameterize interactions between effective spins, $\tilde{\vec{S}}$ (i runs over the four coupled manganese centers; Eq. (7)].

$$\hat{H}_{eff}^{coupled} = \beta\,\vec{B}\,\mathbf{g}\,\tilde{\vec{S}} + \sum_{i=1}^n \tilde{\vec{S}}\,\mathbf{A}_i\,\vec{I}_i + \tilde{\vec{S}}\,\mathbf{D}\,\tilde{\vec{S}} \quad (7)$$

The effective tensors may in turn be related to the isolated (site) tensors of Equation (6) by spin projection. For an $S = {}^1/_2$ ground state, the last ZFS-related term vanishes. We are mainly interested here in the effective HFC tensors $\mathbf{A}_i$. In general, they may be related to the local site tensors $\mathbf{a}_i$ by

Equation (8) in which $\boldsymbol{\rho}_i$ is a spin-projection matrix,[64] which depends on the spin at site i, on the exchange coupling constants of the exchange multiplet, and on the local ZFS tensors.

$$\mathbf{A}_i = \mathbf{a}_i \boldsymbol{\rho}_i \tag{8}$$

The site tensors $\mathbf{a}_i$ in turn are related to the directly computed hyperfine tensors of the BS state $\mathbf{A}_i^{BS}$ by Equation (9) in which, in the present case, $M_S^{BS} = {}^1/_2$ and the sign in the denominator depends on the formal orientation of the local spin in the BS solution.

$$\mathbf{a}_i = \frac{\mathbf{A}_i^{BS} M_S^{BS}}{\pm S_i} \tag{9}$$

For dinuclear $Mn^{III}Mn^{IV}$ complexes, most previous studies have assumed the exchange interaction to be the dominant coupling mechanism between the ions and the ZFS to be negligible[43,44,65] (but see ref. [64]). Then the ZFS terms drop out of the spin-projection matrices, which reduce to scalars. As a first step we will here adopt this assumption, which has also often been made implicitly in spectral simulations for the OEC (however, see ref. [30] and the discussion below). In the case of a dinuclear $Mn^{III}Mn^{IV}$ complex, this "scalar approximation" based on the strong-exchange limit leads to simple spin-projection coefficients c_i given by Equation (10).

$$c_i \equiv c_i(S_i, S_j, S) = \mathbf{A}_i \cdot \mathbf{a}_i^{-1} = \frac{S(S+1) + S_i(S_i+1) - S_j(S_j+1)}{2S(S+1)} \tag{10}$$

For the Mn^{III} site, $c_1 = +2$, and for the Mn^{IV} site, $c_2 = -1$.[43–45] For the spin-coupled $S = {}^1/_2$ states of an $Mn^{III}Mn^{IV}Mn^{IV}Mn^{IV}$ cluster, as in the S_2 state of the OEC, we have always one site with $M_S = +2$ (Mn^{III} site), one with $M_S = +{}^3/_2$, and two with $M_S = -{}^3/_2$ (this is borne out also by computed spin densities of the BS states, see below). In such multinuclear systems, the magnetic interactions have a more complicated topology, as apparent from the numerous parameters J_{ij} in Equation (6). Given that inevitably some spin frustration is involved to reach an $S = {}^1/_2$ state, the exchange-coupling constants may attain very different values and be either negative or positive. Even upon neglecting the ZFS, no full analytical solution is possible anymore for a general tetranuclear system. One either has to diagonalize the Heisenberg–Dirac–van–Vleck (HDvV) Hamiltonian [last term in Eq. (6)] numerically or one may arrive at simplified coupling schemes by imposing certain constraints on the symmetries of the Heisenberg exchange interactions. The first, fully numerical approach was used initially on a synthetic model cluster[66] and subsequently on models of the S_2 state of the OEC by Pantazis et al.[45] Here the (scalar) spin projection coefficients are determined from the ratio given in Equation (11) in which $\langle S_{z,i} \rangle$ is the expectation value at site i of operator $\hat{S}_z$ and is evaluated by using Equation (12) in which C_0^{κ} are the expansion coefficients of the $M_S = +{}^1/_2$ component of the ground doublet state corresponding to the lowest eigenvalue of the HDvV matrix after its diagonalization (label κ enumerates all the possible combinations $S_1 M_{S,1} \ldots, S_n M_{S,n}$, $M_{S,1} = S_i \ldots S_i$).

$$c_i = \frac{\langle S_{z,i} \rangle}{S} \tag{11}$$

$$\langle S_{z,i} \rangle = \sum_{\kappa} \left| C_0^{\kappa} \right|^2 M_{S,i},\ i = 1,\ \ldots\ , n \tag{12}$$

The corresponding matrix elements are constructed in the basis set of spin wave functions $|S_1 M_{S,1} \ldots S_n M_{S,n}\rangle$ within the HDvV Hamiltonian. Therefore, calculation of the spin projection coefficients additionally requires a priori knowledge of the Heisenberg exchange coupling constants, J_{ij}. To extract J_{ij}, we performed a series of broken-symmetry calculations on the $Mn^{III}Mn^{IV}Mn^{IV}Mn^{IV}$ cluster for all possible multiplicities generated by consequently flipping the total spin on each center in addition to the high-spin (HS) state ($S_{HS} = \sum_{i=1}^{4} S_i = {}^{13}/_2$, because $S_1 = 2$, and $S_2 = S_3 = S_4 = {}^3/_2$). All calculations were performed on the optimized structure of the HS state. The parameters J_{ij} are then found from the solution of a system of eight linear equations within the framework of the Ising approximation [Eq. (13)].

$$E(S_K) = -2 \sum_{i<j} M_{S,i} M_{S,j} J_{ij}; M_{S,i} = \pm S_i, \sum_{i=1}^{4} M_{S,i} > 0, K = 13/2,\ 3 \times 7/2,\ 5/2,\ 3 \times 1/2 \tag{13}$$

The series of Equations (13) is overdetermined (eight linearly independent equations with six variables cannot be simultaneously exactly satisfied) and, as in ref. [66], singular value decomposition has been used to find the optimal solution (a simple least-squares fitting algorithm gave numerically indistinguishable results). Analysis of literature data (e.g., ref. [67]) confirmed the validity of the Ising model. In particular, the so-called "spin correlation functions" (i.e., coefficients at J_{ij}) turned out to be very close to the corresponding products $\pm S_i S_j$ (as has been found previously for Ni_9 and 8Fe–7S clusters[62]). Inclusion of ZFS in the spin-projection scheme is outside the scope of this work and will be pursued elsewhere. Possible errors arising from this approximation for the isotropic manganese, nitrogen, and carbon HFCs will be discussed below. For the much smaller hyperfine anisotropies, it is clear that the ZFS-induced transfer of ^{55}Mn HFC anisotropy between the Mn^{III} and Mn^{IV} centers will be significant if the intrinsic $\mathbf{d}_i$ tensors are not all coaxial. Although we will provide full spin-projected HFC tensors in the Supporting Information (obtained with the same scalar spin-projection coefficients c_i as used for the isotropic values), we expect them to be less reliable than the isotropic HFCs. Moreover, we also regard reported ^{55}Mn HFC anisotropies from spectral simulations to be less well defined and we will thus base our discussion mainly on the

isotropic HFCs. Anisotropies will be discussed, however, for the ^{14}N and ^{13}C HFC tensors.

The numerical spin projection scheme of Equations (11)–(13)[45,66] requires the explicit computation of the full set of Heisenberg exchange coupling constants J_{ij} with sufficiently high accuracy (see below). A more approximate scheme, which allows a semi-quantitative estimate of the spin-projection coefficients without the need for explicit prior knowledge of all the J_{ij} values, desirable for a fast screening of a larger number of model systems, has also been evaluated for comparison. Such a simplified scheme becomes possible[51] when the HDvV matrix satisfies certain internal symmetry properties. For instance, in a tetrahedral system of equivalent spins, deviations from the regular tetrahedron down to C_{2v} symmetry will not affect the spin projection. This refers not to spatial symmetry but to internal relations between the J_{ij}. Simplified schemes remain valid as long as certain equalities or inequalities between parameters hold (see below). In contrast to the dinuclear case (see above), for multinuclear systems the actual coupling scheme has to be considered as different states of the same overall spin multiplicity may now be constructed. In the $Mn^{III}(Mn^{IV})_3$ cluster of interest here, as many as seven linearly independent doublet states are possible. However, the construction of the broken-symmetry DFT solutions already allows us to restrict considerations to only two coupling schemes.

Scheme A: A predominant antiferromagnetic interaction couples the "spin-up" Mn^{III} ($S_1=2$) to one of two remaining "spin-down" Mn^{IV} centers (for example, $S_3={}^3/_2$ or $S_4={}^3/_2$; particular indices are given only for illustration purposes) producing an intermediate dimer spin S_{13} (or S_{14}) of ${}^1/_2$. Then the remaining "spin-up" Mn^{IV} ($S_2={}^3/_2$) couples in the same way with "spin-down" Mn^{IV} ($S_4={}^3/_2$ or $S_3={}^3/_2$, respectively) to give zero intermediate spin S_{24} (or S_{23}).

Scheme B: A predominant ferromagnetic interaction couples "spin-up" $S_1=2$ and $S_2={}^3/_2$ to give $S_{12}={}^7/_2$, and the two "spin-down" $S_3={}^3/_2$ and $S_4={}^3/_2$ also couple ferromagnetically to give $S_{34}=3$. The desired doublet state is then obtained by antiferromagnetic coupling of S_{12} and S_{34}.

Scheme A is not unique (one still has to choose between S_3 and S_4, and the final assignment of spin-projection coefficients is ambiguous). It would lead to complete spin compensation and thus zero spin-projection coefficients for the second pair (S_{24} or S_{23}, respectively). That is, the hyperfine couplings for these two "singlet-coupled" centers should vanish, in contradiction to the simulations of the EPR and ENDOR spectra of the S_2 multiline signal (see below). On the other hand, Scheme B is unique, and both S_{12} and S_{34} pairs remain paramagnetic. This will be the preferred scheme in the following. It is supported further by estimates of the properties of the BS solutions (e.g., S^2 expectation values) based on Clebsch–Gordan coefficients. For this Scheme B we have used the appropriate recursion formulae of ref. [51], Equations (14), to obtain approximate spin-projection coefficients (cf. Table 4.6, Eq. (3.23), and Table 3.2 in ref. [51]). The "intermediate coupling" coefficients $c_i(S_i,S_j,S)$ for the dimer fragments are given by Equation (10) (we distinguish capital C_i to represent the spin-projection coefficients for the full cluster).

$$C_1(S_1,S_2,S_{12};S_3,S_4,S_{34};S) = c_1(S_{12},S_{34},S)c_1(S_1,S_2,S_{12}) \quad (14a)$$

$$C_2(S_1,S_2,S_{12};S_3,S_4,S_{34};S) = c_1(S_{12},S_{34},S)[1-c_1(S_1,S_2,S_{12})] \quad (14b)$$

$$C_3(S_1,S_2,S_{12};S_3,S_4,S_{34};S) = [1-c_1(S_{12},S_{34},S)]c_1(S_3,S_4,S_{34}) \quad (14c)$$

$$C_4(S_1,S_2,S_{12};S_3,S_4,S_{34};S) = [1-c_1(S_{12},S_{34},S)][1-c_1(S_3,S_4,S_{34})] \quad (14d)$$

$$C_1 = +{}^{12}/_7,\ C_2 = +{}^9/_7,\ C_3 = C_4 = -1 \quad (15)$$

Substituting $S_1=2$, $S_2=S_3=S_4={}^3/_2$, $S_{12}={}^7/_2$, $S_{34}=3$, and $S={}^1/_2$ (Scheme B) into Equations (10) and (14), one easily obtains Equation (15).

Numerical experiments (see also below) with the full diagonalization scheme of ref. [66] [Eqs. (11)–(13)] suggest that spin-projection coefficients similar to those of Equation (15) are in fact obtained to a good approximation in a rather wide range of relative parameter values provided that certain relationships are fulfilled: 1) Both J_{12} and J_{34} are either positive or, at least, less negative than the remaining exchange coupling constants (thus justifying predominant ferromagnetic coupling between spins 1 and 2, and between 3 and 4, as required by Scheme B) and 2) $J_{13}\approx J_{23}$ and $J_{14}\approx J_{24}$. This reduces the number of different exchange coupling constants. Even if condition (2) is only fulfilled crudely, the final spin-projection coefficients deviate at most by a few percent from those in Equation (15). Note that the spin-projection coefficients from Equation (15) are obtained exactly, irrespective of the actual values of the exchange-coupling constants if $J_{13}=J_{23}=J_I<0$; $J_{14}=J_{24}=J_{II}<0$; $J_{12},J_{34}>J_I$; $J_{12},J_{34}>J_{II}$. We will discuss the validity of these approximations further below for the two main model clusters studied.

Construction of Model Systems

We will focus on the two model systems shown in Figure 1 and will mention results for other models only in passing (cf. also the Supporting Information). Evaluation of the cluster model **SG2009^{-1}** from ref. [47] (Figure 1, left) is most interesting given its energetic superiority relative to other models proposed in the literature[46] (see the Introduction). It is related to the models **11** and **12** studied in ref. [45] except that the protein residues are slightly more truncated (truncation sites were saturated by hydrogen atoms, the positions of which were optimized). In our experience, the level of truncation used does not affect the intrinsic HFCs and simplifies analyses. To make sure that the spin projection is not affected, we have also computed the exchange coupling constants explicitly for the larger models **11** and **12**

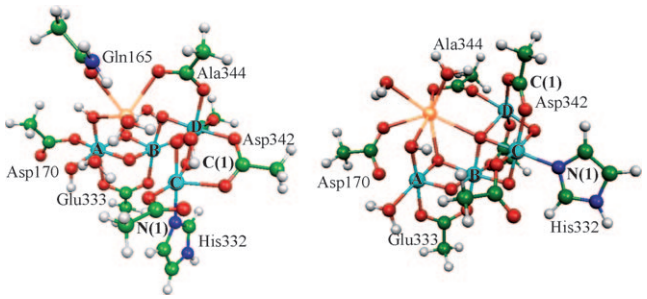

Figure 1. Two model systems of the S_2 state: **SG2009^{-1}** (left) and **YII-1^0** (right). Assignments of specific amino acid residues to certain binding sites on the cluster are partly tentative (see discussion below regarding D1-Ala344 binding modes).

(see below). The coordinates were taken directly from ref. [47]. They are based on unrestricted B3LYP*/lacvp* optimization of the HS state in a surrounding dielectric medium with dielectric constant 6.0 (for further details, see ref. [47]).

Among the models with "twisted-pair topology", we have selected as the most promising for closer comparison model **YII-1^0** (Figure 1, right) from a larger number of models based on EXAFS and/or X-ray data. It is derived from the core IIa structure based on the polarized high-resolution EXAFS studies of Yano et al.[24] on oriented PSII membranes or single crystals and is thus most closely related to model **3** of ref. [45]. In the initial stages of the present work, we combined the three basic cores of ref. [24] with ligand environments deduced from X-ray structures determined at resolutions of 3.0[11] and 3.5 Å.[9] The resulting ligand spheres are similar but not identical to those used by Pantazis et al. (in fact, ref. [45] appeared after our first EPR calculations on these systems). Moreover, in contrast to ref. [45], the structure has been fully optimized without constraints on the manganese and calcium positions. Seven amino acid residues are directly coordinated. Only two carboxylato ligands are bound terminally, the others bridge two manganese centers or a manganese and calcium. Thus, only four water-derived ligands are needed to complete the coordination. No chloride ions have been included. A model similar to **YII-1^0** has recently been studied by further quantum-chemical calculations.[68,69] It differs mainly by having one less water ligand on the calcium atom.

Coordinates of the two models can be found in Table S1 in the Supporting Information. Data for other models based on the three twisted-core structures of ref. [24] and for a few other models are compared and discussed in the Supporting Information (Section S1, Table S1, and Figure S1).

Computational Details

Structure optimizations of model **YII-1^0**, and of the additional models given in the Supporting Information, were performed by using the Turbomole 5.9.1 code.[70] Based on the initial coordinates obtained, as described above, the full structure optimizations employed the B3LYP[71,72] hybrid functional with SVP basis sets[73] and unrestricted Kohn–Sham wavefunctions. We have been able to construct various different BS states for all models in addition to the HS state. With suitable initial-guess wavefunctions, the states remained stable, as confirmed by Mulliken spin-density analyses (see below). It was thus possible to optimize all these different states separately. However, after many test calculations, we decided to compute all the exchange coupling constants and hyperfine tensors for the optimized HS structure. Use of identical structures for the different spin states is consistent with the subsequent application of the HDvV Hamiltonian for spin projection.

At these optimized structures, as well as for model **SG2009^{-1}** (see above), unrestricted Kohn–Sham single-point calculations of the relative energies of different BS and HS states and of the HFC tensors were performed with Turbomole by using a 9s7p4d basis set for manganese (specifically designed for hyperfine calculations[73–75]) and flexible IGLO-II[76,77] basis sets for the ligand atoms. Previous computational studies on both mono-[78] and dinuclear[43–44,65] manganese complexes have indicated that B3LYP calculations provide reasonable agreement with experiment for the manganese HFC anisotropies and for the ligand EPR parameters. Isotropic transition-metal hyperfine couplings are typically underestimated in absolute values at this level due to an insufficient description of core-shell spin polarization.[74,75] Fortunately, the deviations for the isotropic manganese HFCs turned out to be systematic[43,44,65,79] and may be corrected by scaling the computed results with a factor of 1.45[65] (similar scaling factors have been used by Pantazis et al. at the B3LYP level,[66] different factors have been employed for different functionals). For calculation of the Heisenberg exchange coupling constants discussed in the context of spin-projection schemes (see below), we have used both B3LYP and the meta-GGA hybrid functional TPSSh[79] as the latter has been singled out from a number of functionals by Pantazis et al.[66]

The unrestricted Kohn–Sham orbitals were transferred to the MAG-Respect property package[80] by suitable interface routines to compute the HFC and NQC parameters. The atomic mean-field approximation (AMFI)[81,82] was used to compute the matrix elements of the Breit–Pauli SO operator for the SO corrections to the manganese HFC tensors [cf. Eq. (3)]. Mulliken spin-density analyses were used to verify convergence to the proper BS and HS states. Spin-density isosurfaces were computed and displayed by using the Molekel program.[83]

Results and Discussion

Exchange coupling constants, spin-coupling schemes, and energy spectra: Figure 2 shows for both models the spin configurations and spin-density distributions of the HS state and of the three BS states with $S = {}^1/_2$. Although the energies of the BS states are very similar (the relative energies for all relevant BS and HS states are given in Table S2 in the Supporting Information), the calculations generally gave a clear preference for a certain distribution of the three Mn^{IV} and single Mn^{III} oxidation states. For model **SG2009^{-1}**, the unique Mn^{III} center is Mn_C (cf. Figure 1). In ref. [45] this assignment for the closely related models **11** and **12** was made to Mn_D, but this arises from different labeling: We prefer to assign Mn_C consistently to the center to which D1-His332 is coordinated. For **YII-1^0**, Mn^{III} is Mn_D, consistent with the results of Pantazis et al.[45] for all EXAFS-based twisted-core models (our calculations also agree with this for the other twisted-core models, see Section S1 in the Supporting Information). The spin-coupling patterns are nicely confirmed by the spin-density plots (Figure 2) as well as by computed Mulliken atomic spin densities (provided below in Table 3).

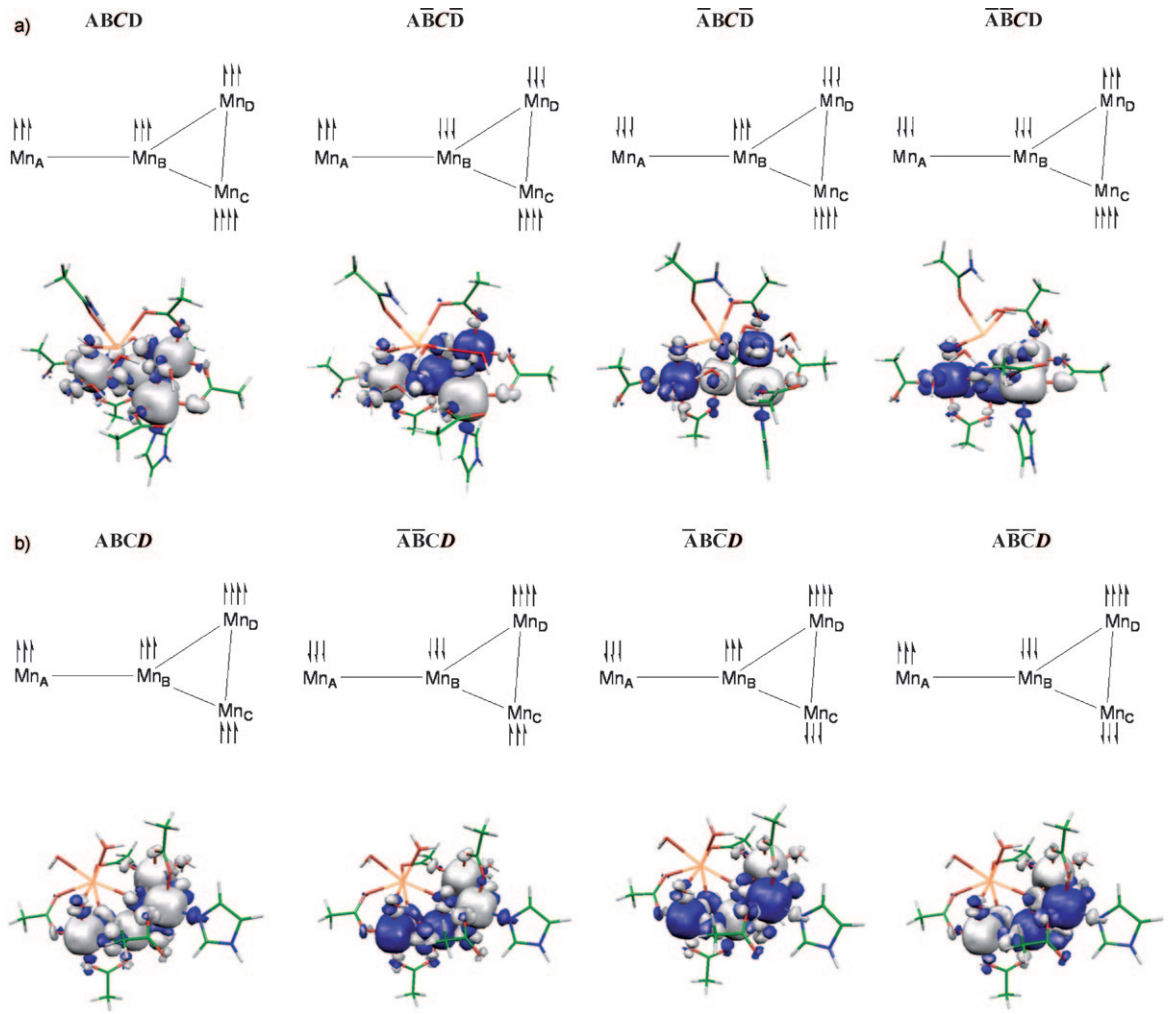

Figure 2. Spin configurations and spin-density distributions (isosurfaces ±0.003 a.u.) for HS ($S=^{13}/_{2}$) and BS ($S=^{1}/_{2}$) states. The shorthand notation for the spin configurations uses a horizontal bar to indicate "spin down" on the given center and italics to specify the Mn^{III} d^4 center. a) Model **SG2009^{-1}**. b) Model **YII-1^{0}**.

The Heisenberg coupling constants J_{ij}, obtained from Equation (13), and the energies of the low-lying excited states, obtained after diagonalization of the HDvV matrix, are given in Table 1. Results based on B3LYP and TPSSh are compared. In their recent work on a synthetic model complex, Pantazis et al.[66] singled out the TPSSh functional as superior to, for example, pure GGA functionals or PBE0 in computing these quantities, but the differences between B3LYP and TPSSh for exchange coupling constants and energy spectra were small. Indeed, both functionals provide qualitatively similar exchange coupling constants and coupling patterns for a given model, with a maximum deviation of 2 cm^{-1} for **SG2009^{-1}** and of 9 cm^{-1} (J_{BC}) for **YII-1^{0}**. The character of the ground state of a given model is also unaffected by the choice of functional. However, the energy spectra are somewhat more influenced: For **SG2009^{-1}**, B3LYP gives smaller energy separations than TPSSh, whereas the situation is reversed for **YII-1^{0}** (Table 1). In general, the energy gap to the lowest excited state (generally $S=^{3}/_{2}$ for both models) is only a few cm^{-1} with both functionals,

Table 1. Calculated exchange coupling constants, J, and energies of different multiplets relative to the doublet ground state for models **SG2009^{-1}** and **YII-1^{0}**.[a]

		Heisenberg coupling constants [cm^{-1}]					
		J_{AB}	J_{AC}	J_{AD}	J_{BC}	J_{BD}	J_{CD}
SG2009^{-1}	B3LYP	0	5	3	8	22	−31
	TPSSh	−2	4	3	9	22	−33
YII-1^{0}	B3LYP	10	4	−1	−22	−18	13
	TPSSh	7	5	−2	−31	−26	8
		Spin-state energies relative to ground state [cm^{-1}]					
SG2009	B3LYP	$S=^{1}/_{2}$	$S=^{3}/_{2}$	$S=^{5}/_{2}$	$S=^{7}/_{2}$	$S=^{5}/_{2}$	$S=^{5}/_{2}$
		0	1.2	3.8	9.5	33.0	34.8
	TPSSh	$S=^{1}/_{2}$	$S=^{3}/_{2}$	$S=^{5}/_{2}$	$S=^{1}/_{2}$	$S=^{7}/_{2}$	$S=^{3}/_{2}$
		0	4.0	11.6	23.3	23.9	31.1
YII-1	B3LYP	$S=^{1}/_{2}$	$S=^{3}/_{2}$	$S=^{5}/_{2}$	$S=^{7}/_{2}$	$S=^{9}/_{2}$	$S=^{1}/_{2}$
		0	6.3	18.4	39.5	132.2	148.4
	TPSSh	$S=^{1}/_{2}$	$S=^{3}/_{2}$	$S=^{5}/_{2}$	$S=^{7}/_{2}$	$S=^{1}/_{2}$	$S=^{3}/_{2}$
		0	4.2	12.9	28.6	137.5	147.9

[a] Obtained from SVD fit of the HDvV matrix and subsequent diagonalization, see the Theory section.

much smaller than the approximate 35 cm^{-1} elucidated by EPR saturation and temperature-dependence studies.[34,84,85] The resulting exchange coupling constants are also much smaller than found, for example, for dinuclear $Mn^{III}Mn^{IV}$ complexes.[65] This is understandable for both geometrical arrangements from the unavoidable spin frustration for the given spin couplings and an $S=1/2$ ground state. The energy separations to the lowest excited state, obtained by Pantazis et al. at the TPSSh level for the various models studied, range from 3 to 92 cm^{-1} (up to 78 cm^{-1} for systems with an $S=1/2$ ground state).[45] Moreover, in some cases the ground state obtained after fitting the HDvV matrix was not a doublet. This shows that the spin-coupling patterns depend crucially on rather small structural details. In the synthetic model complex studied earlier by Pantazis et al.,[66] larger antiferromagnetic couplings and less low-lying excited states were computed. This likely reflects the somewhat more open structure of that cluster.

The structures of the two model complexes (Figure 1) provide indications of the origin of the different preferred manganese oxidation-state distributions: In **SG2009^{-1}**, Mn_C has an open coordination site *trans* to the carboxylato ligand (Figure 1), which in mechanistic considerations acts as a water binding site. This favors creation of the Mn^{III} center at this five-coordinate Mn_C site. In model **YII-1^0**, Mn_D is five-coordinate and the site of Mn^{III}, albeit coordination of a water molecule to this site does not alter the oxidation-state distribution (cf. model **YII-2^0** in Section S1 in the Supporting Information).

Closer examination and comparison of the exchange coupling constants for the two models (and for the models of ref. [45]) reveal a number of interesting points. Structural arguments (cf. Figure 1) suggest near zero values for J_{AC} and J_{AD} as the dangler Mn_A is remote from Mn_C and Mn_D. These exchange coupling constants are indeed small (also for most of the models in ref. [45]). For model **YII-1^0**, we see J_{AB} and J_{CD} as the two most positive exchange couplings (the latter involves the Mn^{III} center), independent of the functional, whereas the clearly most negative values are J_{BC} and J_{BD}. This Y-shaped pattern is not only consistent with the structure of the model, but also with the qualitative spin-projection Scheme B outlined in the Theory section. That is, we expect spin-projection coefficients close to the idealized ones in Equation (15), as is indeed found (see below). In contrast, only one clearly antiferromagnetic coupling (J_{CD}) is found for model **SG2009^{-1}** and no clear S_{12}/S_{34} pattern, as required by Scheme B, is present. This points to even larger spin frustration in this model, consistent with the even smaller energy differences to the lowest excited states (Table 1). We note that the slightly larger, closely related model **11** of ref. [45] also gives a doublet ground state but slightly different exchange couplings, whereas the even larger model **12** does not provide a doublet ground state (cf. Table S3 in the Supporting Information). Clearly, the very small energy spacings between the BS and HS states, and thus the results of diagonalizing the HDvV Hamiltonian, are sensitive to small modifications of the models.

In dinuclear $Mn^{III}Mn^{IV}$ complexes, bis-μ-oxo-carboxylato bridges like those computed in both models between Mn_C and Mn_D (and between Mn_A and Mn_B) usually give rise to exchange coupling constants close to -100 cm^{-1}.[65] The present observation of much smaller absolute Heisenberg coupling constants for the tetranuclear OEC models relative to most $Mn^{III}Mn^{IV}$ dinuclear $S=1/2$ complexes with similar bridging ligand sets is most notable and is also consistent with the values for most models in ref. [45] (the largest absolute value for any exchange coupling constant for an $S=1/2$ ground state in ref. [45] is $J_{AB}=48$ cm^{-1} for model **1**, which has no carboxylato bridge between Mn_A and Mn_B). We expect that this is an intrinsic feature of the spin frustration in the S_2 state and that further refinements of the models will most likely not change this picture fundamentally. This observation has significant consequences for the interpretation of the EPR spectra. For example, in ref. [34], a structure filter for acceptable spin coupling patterns assumed J_{AB} to be between -250 and -100 cm^{-1}. This assumption (and some further assumptions for other exchange couplings) is clearly not borne out by the computed patterns for any of the models studied here or in ref. [45]. Other simulations for the S_2 state also assumed far larger antiferromagnetic couplings than found here,[30] which led to a number of structural conclusions (favoring a dangler model). The present values for J_{AB} are either slightly positive (**YII-1^0**) or close to zero (**SG2009^{-1}**). Although Pantazis et al. attributed the small J_{AB} values for most models with hydrogen bonding to one of the μ-oxo bridges between Mn_A and Mn_B,[45] we note that no such hydrogen bonding is present in **YII-1^0**. Only the very unlikely model **1** in ref. [45] gave a somewhat larger antiferromagnetic Mn_A–Mn_B coupling ($J_{AB}=-48$ cm^{-1}). The transfer of certain observations concerning Heisenberg exchange coupling constants from dinuclear systems to the OEC thus has to be viewed critically. We also note that **YII-1^0** has a positive J_{AB} but nevertheless exhibits an $S=1/2$ ground state, contrary to observations made in ref. [45].

Another point raised by the computed exchange coupling constants pertains to the strong exchange limit implied by the spin-projection scheme used here (see the Theory section) and by Pantazis et al.,[45,66] and implicitly also in the discussion of ref. [34]. The neglect of ZFS contributions for the spin projection of the isotropic HFCs becomes a questionable approximation in view of the small values of J_{ij}, as conceded in ref. [45]. For a dinuclear $Mn^{III}Mn^{IV}$ system, Orio et al.[86] recently estimated that for absolute exchange couplings of less than 75 cm^{-1}, neglect of ZFS (with typical values of d_i for Mn^{III} between 1 and 4 cm^{-1}) in the spin projection may lead to significant errors in the computed ^{55}Mn HFCs (see also the earlier work of Zheng et al.[64]). Given the overall small energy separations, none of the models studied here or in ref. [45] is safely on the strong-exchange side. This has to be borne in mind when considering the reliability of spin-projection schemes assuming a strong exchange limit (see below).

Spin-projection coefficients: With these limitations in mind, we focus on the spin-projection coefficients (Table 2) obtained from the numerical scheme[66] of Equations (11)–(13)

Table 2. Calculated on-site spin expectation coefficients C_i for models **SG2009**$^{-1}$ and **YII-1**^{0}.

		Mn_A	Mn_B	Mn_C	Mn_D	Coupling
SG2009^{-1}	B3LYP[a]	+1.512	−0.995	+1.270	−0.786	$A\bar{B}C\bar{D}$
	TPSSh[a]	+1.368	−0.987	+1.477	−0.857	
	Eq. (15)[b]	+1.286	−1.000	+1.714	−1.000	
YII-1^{0}	B3LYP[a]	−0.996	−1.000	+1.312	+1.682	$\bar{A}\bar{B}CD$
	TPSSh[a]	−0.990	−1.000	+1.339	+1.651	
	Eq. (15)[b]	−1.000	−1.000	+1.286	+1.714	

[a] Spin-projection coefficients obtained numerically from Equations (11)–(13). [b] Simplified spin-projection coefficients from Equation (15).

with J_{ij} values from either B3LYP or TPSSh calculations and compare them with the coefficients from the simpler scheme of Equation (15), which does not require the explicit calculation of exchange couplings. We note first of all that for both structural models spin-coupling schemes in agreement with Figure 2 and a doublet ground state are obtained irrespective of the functional (see above). As expected from the pattern of the exchange couplings in **YII-1**^{0} (see above and Table 1), the numerically computed spin-projection coefficients for this model are very close to the idealized values derived from Equation (15) with both functionals. This indicates a topologically stable situation in which the small differences between the exchange coupling constants (cf. Table 1) for the different functionals do not affect the spin-projection coefficients much.

The situation is different for the topologically less clear-cut distribution (see above) of exchange coupling constants in **SG2009**$^{-1}$. Here, in particular, the spin-projection coefficients for the "spin-up" sites Mn_A and Mn_C show a large dependence on the functional. At the TPSSh level, the coefficients for these two centers agree qualitatively and semiquantitatively with the topology intrinsic to Equation (15), with the larger spin-projection coefficient for the Mn^{III} site (Mn_C), that is, $C_C > C_A$. The B3LYP exchange coupling constants, in contrast, give $C_A > C_C$ [Table 2; with both functionals, C_B is close to −1 as predicted by Equation (15), whereas C_D deviates somewhat more]. This indicates a very large sensitivity of the numerically computed spin-projection coefficients to very small changes in the Heisenberg coupling constants for **SG2009**$^{-1}$, but not for **YII-1**^{0}. The largest difference in an exchange coupling constant for **SG2009**$^{-1}$ between B3LYP and TPSSh is only 2 cm^{-1}, yet the spin-projection coefficients change notably. As J_{AB} exhibits the largest change on a relative scale, we have varied this constant over a larger range of around ±10 cm^{-1} while keeping the other J_{ij} values fixed to the TPSSh results. When setting J_{AB} to 0 cm^{-1}, as obtained with B3LYP, we obtain C_i values of +1.492, −0.999, +1.281, and −0.794, that is, close to the B3LYP data, with $C_A > C_C$. That is, a change in the one exchange coupling constant by only 2 cm^{-1} may change the spin-projection coefficients drastically. In contrast, $J_{AB} = -5$ cm^{-1} gives coefficients of +1.180, −0.925, +1.677, and −0.932, close to the idealized values deduced from Equation (15). It is also possible to judge the sensitivity of the spin-projection coefficients to changes in the exchange coupling constants by computing partial derivatives (provided in Table S4 in the Supporting Information). The results confirm a significantly larger dependence of the spin projection on the exchange couplings for **SG2009**$^{-1}$ relative to **YII-1**^{0} and furthermore give an idea of the dependencies of specific spin-projection coefficients on specific exchange couplings. We note in passing that the slightly larger model **11** from ref. [45] again presents a more stable situation, with computed spin-projection coefficients near those deduced from Equation (15) for both B3LYP and TPSSh results (Table S3 in the Supporting Information).

We may thus ask if the HDvV Hamiltonian obtained by fitting to the results of BS-DFT calculations is sufficiently accurate to obtain numerically reliable spin-projection coefficients. It seems that the answer to this question depends on the topological stability of the spin-coupling pattern for a given structural model. Note that the energy gap to the lowest-lying excited spin state ($S = {}^3/_2$) is computed to be too small in comparison with experimental estimates for both functionals and both models (see above and Table 1). How much would the exchange coupling constants have to change to find agreement with these experiments? Not much in fact. For the spin-coupling topology and oxidation-state distribution of the **SG2009**$^{-1}$ model, idealized exchange coupling constants of $J_{AB} = -15$, $J_{BD} = +20$, $J_{CD} = -20$, and $J_{AC} = J_{AD} = J_{BC} = 0$ (in cm^{-1}) would give a lowest-energy gap of 28.7 cm^{-1}, close to the experimental value of around 35 cm^{-1}. For the topology of **YII-1**^{0}, an idealized coupling pattern of $J_{AB} = J_{CD} = +30$, $J_{BC} = J_{BD} = -30$, and $J_{AC} = J_{AD} = 0$ (in cm^{-1}) would provide a gap of 24.1 cm^{-1}, also close to the experimental value. Both of these coupling schemes require only relatively moderate changes in the exchange coupling constants compared with the actually computed values but provide improved energy gaps and spin-projection coefficients close to those of Equation (15).

We thus conclude that for complicated spin-coupled clusters like those treated here, with very low-lying excited states, the currently available accuracy of BS-DFT calculations is not sufficiently high to derive in all cases very reliable Heisenberg coupling constants and therefore spin-projection coefficients from Equations (11)–(13) or to predict the energy spectrum of the excited states with very high accuracy. Apart from the limitations of the accuracy of the BS-DFT approach itself (functionals, basis sets), we have to take into account (see the discussion above) that the inclusion of ZFS in the spin-projection scheme might affect the computed hyperfine tensors more than differences between the numerically computed spin-projection coefficients derived from Equations (11)–(13) and the simplified ones from Equation (15).

In the following discussion of hyperfine couplings, we thus will prefer the simpler scheme based on Equation (15) for

the spin projection. At the present level of accuracy of BS-DFT calculations, we expect no significant loss of reliability of computed hyperfine couplings in comparison with the numerical procedure of refs. [45,66]. The simpler scheme has the advantage of not requiring extra computations of intermediate spin BS states and the numerical schemes of Equations (11)–(13). We emphasize that this does not invalidate the full numerical fit, which is clearly the more complete procedure provided that very accurate Heisenberg exchange couplings are available. Moreover, inclusion of ZFS precludes simplifying assumptions based on spin topology and will require a start from the full numerical treatment in any case.

^{55}Mn hyperfine couplings: As discussed in the Theory section, the very small manganese HFC anisotropies may be critically affected by the neglect of the ZFS and are not expected to be very reliable. We note in passing that only the computed anisotropies of the Mn^{III} site are significant (Table S5 in the Supporting Information), whereas in the simulations of the experimental spectra, the anisotropy is more spread out towards the Mn^{IV} centers, possibly due to ZFS-related anisotropy transfer neglected in the present calculations. While work on extended spin-projection schemes including ZFS is ongoing, in its absence we will here concentrate on the computed isotropic HFCs, which are summarized in Table 3 (scaled B3LYP results), for our two central model complexes, comparing in both cases the three possible $S=^1/_2$ BS states. The spin projection is based on Equation (15), that is, $c_1=^{12}/_7$ ($M_{S,1}=+2$), $c_2=^9/_7$ ($M_{S,2}=+^3/_2$), $c_3=c_4=-1$ ($M_{S,3}=M_{S,4}=-^3/_2$). By using these generic spin-projection coefficients, we have computed HFCs for all three $S=^1/_2$ BS states of a given model. This allows further insights into the dependence on the spin-coupling patterns.

Comparison with experiment should be made for A_{iso}*, empirically scaled by 1.45 (see the Computational Details section).[65] We note in passing that spin–orbit corrections to the isotropic HFCs (A^{PC}) are non-negligible, in the range of 5–10% of the nonrelativistic Fermi contact term (A^{FC}), a typical magnitude for manganese HFCs.[43,44,65,78] Scaled site values a_{iso}* are also given to see how the spin densities of Mn^{III} and Mn^{IV} centers (see last column in Table 3 for Mulliken spin densities) correlate with the intrinsic hyperfine values.

Three different sets of experimental HFC tensors obtained in different simulations of the EPR and ENDOR spectra are also given.[30–32] Their differences reflect not only the different way in which the simulations were performed, but also, in part, aspects of sample preparation. We thus regard these data (Table 3) for the moment as a range to compare with. All three sets feature one HFC near 300 MHz. Two of the sets have two HFCs near 200 MHz and one near 250 MHz,[30,31] whereas the data of Charlot et al.[32] feature two HFCs near 250 MHz and only one near 200 MHz. Neither sign information nor any assignment of the HFCs to specific manganese centers can be derived with certainty experimentally. The additional value of 312 MHz of Teutloff et al.,[87] determined from single-crystal Q-band ENDOR experiments, refers specifically to the largest HFC (see also Table S5 for the corresponding tensor). We note in passing that even a change in species from spinach to *Th. elongatus* PSII or treatment with MeOH may visibly affect

Table 3. Computed ^{55}Mn hyperfine tensors (in MHz) for different broken-symmetry states of models **SG2009^{-1}** and **YII-1^0** and compared with the results of EPR/ENDOR simulations.[a]

	BS state (ΔE)[b]		a_{iso}*(site)	A_{iso}*	A_{iso}	A_{FC}	A_{PC}	$\rho^{\alpha-\beta}$
SG2009^{-1}	$A\bar{B}C\bar{D}$	A	−233	−299	−206	−191	−15	2.93
	(0)	B	−191	191	132	120	12	−2.89
		C	−151	−259	−179	−167	−12	3.93
		D	−222	222	153	141	12	−2.97
	$A\bar{B}\bar{C}D$	A	−236	236	163	151	12	−2.91
	(134)	B	−235	−302	−208	−193	−15	2.85
		C	−144	−247	−170	−159	−12	3.93
		D	−243	243	168	156	12	−2.96
	$\bar{A}\bar{B}CD$	A	−180	180	124	113	12	−2.95
	(619)	B	−201	201	139	127	12	−2.87
		C	−100	−171	−118	−106	−12	3.92
		D	−191	−245	−169	−154	−15	2.99
YII-1	$A\bar{B}\bar{C}D$	A	−219	−282	−195	−179	−15	2.95
	(0)	B	−207	207	143	130	13	−2.92
		C	−190	190	131	119	12	−2.99
		D	−187	−321	−222	−210	−12	3.84
	$\bar{A}B\bar{C}D$	A	−222	222	153	141	12	−2.90
	(401)	B	−262	−337	−232	−216	−16	2.91
		C	−243	243	168	156	12	−2.84
		D	−178	−305	−210	−198	−12	3.80
	$\bar{A}\bar{B}CD$	A	−181	181	125	114	11	2.90
	(702)	B	−199	199	137	124	−12	−2.84
		C	−219	−281	−194	−179	−15	2.94
		D	−154	−264	−182	−170	−11	3.80
exp.								
Kulik et al.[c]		1		193				
		2		205				
		3		245				
		4		295				
Peloquin et al.[d]		1		245				
		2		200				
		3		297				
		4		217				
Charlot et al.[e]		1		186				
		2		243				
		3		257				
		4		329				
Teutloff et al.[f]				312				

[a] A_{iso}* is the isotropic HFC after spin projection [according to the spin-projection coefficients in Eq. (15)] and scaling by the empirical factor of 1.45 (cf. Computational Details), a_{iso}* is the corresponding scaled site value. A_{FC} and A_{PC} are the isotropic first-order Fermi contact and the second-order pseudo-contact (spin–orbit) contributions to A_{iso}. $\rho^{\alpha-\beta}$ is the Mulliken spin density at the manganese atom. [b] Spin-coupling pattern of the BS states and energy relative to the lowest computed BS state (in cm^{-1}) for a given model. [c] Simulation results from ref. [31]. [d] Simulation results from ref. [30]. [e] Simulation results from ref. [32]. [f] HFC for the site with the largest isotropic value, as obtained from the simulation of single-crystal Q-band ^{55}Mn ENDOR for PSII from *Th. elongatus*.[87]

the splitting in the spectra in the order of about 10 MHz for a given site.[87]

Examining first the site values, we note that the Mn^{III} site (Mn_C for **SG2009^{-1}**, Mn_D for **YII-1^0**) provides in fact the smallest absolute a_{iso}*, in spite of the largest absolute site spin density at this center (Table 3). This most likely arises from some s character and thus direct contributions to the spin density at the nucleus for this structurally distorted, five-coordinate center.[75] Small intrinsic site values for pentacoordinated manganese sites have also been found computationally for dinuclear $Mn^{III}Mn^{IV}$ complexes.[65] As the Mn^{III} site is projected with the largest spin-projection coefficient ($+^{12}/_{7}$), the corresponding projected A_{iso}* is not the smallest absolute value anymore for most states, but it also does not necessarily have to be the largest HFC. In fact, it turns out to be the largest value for the lowest BS state of **YII-1^0**, but only the second largest for the lowest BS state of **SG2009^{-1}**. This seems to be a notable result as it puts into question the generally made assumption that the largest isotropic HFC of the S_2 state pertains necessarily to the Mn^{III} site. The different BS states for a given model provide somewhat different patterns of HFCs, albeit the absolute values for the two lowest-energy states do not differ very much ($A\bar{B}C\bar{D}$ and $\bar{A}BC\bar{D}$ for **SG2009^{-1}**, $A\bar{B}\bar{C}D$ and $\bar{A}B\bar{C}D$ for **YII-1^0**). Taking the lowest-energy BS state for both models provides HFCs in reasonable agreement with the experimental range. In fact, **SG2009^{-1}** then provides almost perfect agreement with the results of simulations presented in refs. [30,31], with one HFC near 300 MHz, one near 250 Hz, and two near 200 MHz, whereas **YII-1^0** exhibits two HFCs in the 300 MHz range. For the other models studied, results for the lowest-energy BS state are summarized in Table S6 in the Supporting Information. Some models give agreement with experiment that is similar to that of the two models studied here in greater detail. The other twisted-core models give values close to 400 MHz for Mn_D, likely due to a six-coordination at this center, in contrast to model **YII-1^0** selected here for closer scrutiny (most models in ref. [45] also gave one larger value). None of the other models provides better agreement than the energy-competitive model **SG2009^{-1}**. However, in view of the approximations involved currently in the spin projection (see the discussion above), one should probably not over-rate the significance of the exact values obtained.

Histidine ^{14}N EPR parameters: As the computed isotropic ^{55}Mn HFCs currently do not seem to provide sufficiently diagnostic probes at the current level of spin projection to distinguish between different structural models, we have extended the study to the histidine (D1-His332) ^{14}N EPR parameters (for N1 directly coordinating Mn_C). Notably, model **SG2009^{-1}** has the histidine bound to the Mn^{III} center (Figure 1), in contrast to all other models studied here or in ref. [45]. It is therefore of interest to explore whether the computed HFC and NQC tensors provide a means of distinguishing between a histidine bound to an Mn^{III} or Mn^{IV} center. Experimentally, Yeagle et al. found that, depending on the projection factors, the observed ^{14}N HFC could be assigned to either an Mn^{III} or an Mn^{IV} site, but the latter required more unusual intrinsic site values.[39] No sign information has been deduced so far. Previous computations on dinuclear $Mn^{III}Mn^{IV}$ systems suggested that B3LYP without any scaling should provide reasonable ^{14}N HFCs and NQC parameters after spin projection.[43,65] The isotropic nitrogen HFC depends both on SOMO spin delocalization onto s-type valence orbitals on nitrogen and on spin polarization, two effects that may not necessarily move in the same direction in different bonding situations. It is thus more difficult to describe accurately than HFC anisotropy. The histidine is modeled by an imidazole, which according to our experience[88] should provide sufficiently accurate EPR parameters for the directly coordinating N1 atom.

Model **SG2009^{-1}** exhibits a smaller absolute isotropic site value than **YII-1^0**, but due to a larger spin-projection coefficient ($+^{12}/_{7}$ for Mn^{III} compared with -1 for spin-down Mn^{IV}), the projected values are almost the same, about 4 MHz. This is too small in comparison with the approximate 7 MHz available from the ESEEM data. We may compare this to our previous calculations on manganese catalase at the same computational level,[65] which provided an absolute ^{14}N A_{iso} value of 4.7 MHz and may be compared with the recent experimental value of 5.75 MHz[89] (for *Lactobacillus plantarum*). There is a tendency for too small isotropic HFCs to be also computed for the other models examined (see Table S7 in the Supporting Information), albeit one of the dangler models (**F-2^{+1}**) and two of the twisted-core models give somewhat larger A_{iso} values close to 6 MHz.

Strikingly, however, model **SG2009^{-1}** is the only one (Tables 4 and S7) that provides a reasonable ^{14}N hyperfine anisotropy. All other models give anisotropies lower by more than a factor 2, including **YII-1^0**. Note that the available ESEEM experiments have been simulated by axially symmetrical HFC tensors,[38,39] but the spectra do not exclude rhombic tensors as found computationally. The larger anisotropy for **SG2009^{-1}** compared with the other models is in part due to the larger projection factor for the Mn^{III} center and partly to a larger intrinsic anisotropy, consistent

Table 4. Comparison of the computed ^{14}N HFC and NQC tensors with ESEEM data (in MHz).[a]

	BS state	a_{iso}(site)	A_{iso}	T_1	T_2	T_3	e^2qQ/h	$\lvert\eta\rvert$	$\rho^{\alpha-\beta}$
SG2009^{-1}	$A\bar{B}C\bar{D}$	−2.2	−3.8	−0.8	−0.5	1.2	−2.66	0.56	−0.04
YII-1^0	$A\bar{B}\bar{C}D$	−4.2	4.2	−0.4	0.1	0.2	1.91	0.99	0.05
exp.[b]			7.4	−0.63	−0.63	1.26	2.3	0.8	
exp.[c]			7.3 ± 0.20	−0.5 ± 0.10	−0.5 ± 0.10	1.0 ± 0.20	1.98 ± 0.05	0.84 ± 0.06	

[a] Spin projection of the HFCs using the spin-projection coefficients of Equation (15), that is, $+^{12}/_{7}$ for **SG2009^{-1}** and -1 for **YII-1^0**. [b] Simulations based on Q- and K_a-band ESEEM data[38] (no error bars given). [c] Simulations based on X-, P-, and K_a-band ESEEM data.[39]

with recent calculations on dinuclear $Mn^{III}Mn^{IV}$ complexes in which clearly larger anisotropies of the nitrogen hyperfine tensors were found for ligands bound to the Mn^{III} than to the Mn^{IV} center.[65] Very recent ESEEM results for two dimanganese catalases identified two histidine ligands coordinated to manganese, one to the Mn^{IV}, and one to the Mn^{III} center.[89] In this case, both the larger A_{iso} and A_{dip} were assigned to the Mn^{III} site. These results for the ^{14}N HFC tensors are thus consistent with the histidine being bound to the unique Mn^{III} center, as suggested by the ESEEM results.[39] Although we bear in mind the approximate spin projection (neglect of ZFS), this agreement is further support for the energetically favorable model **SG2009^{-1}** as this is the only one of those considered so far that is computed to have Mn^{III} at the Mn_C site. Notably, in the most recently suggested reaction mechanism associated with the model, Mn_C is the center that binds an external water molecule and is oxidized to Mn^{IV} during the S_2–S_3 reconstruction step and the site at which a crucial oxygen radical is formed in the S_3–S_4 transition.

The nuclear quadrupole coupling constant e^2qQ/h is reproduced well by all models (Tables 4 and S7, with **SG2009^{-1}** too high and the other models too low by about 0.4 MHz) and it is in a similar range as found for superoxidized dimanganese catalase[90] and for other imidazole imino nitrogen atoms coordinated to metal centers.[91] The asymmetry parameter $|\eta|$ is less well reproduced. The experimental value of around 0.8 is larger than for dimanganese catalase[90] and other metal-coordinated imidazole ligands.[91] Model **SG2009^{-1}** gives a lower value and model **YII-1^0** a higher one (Table 4). The other models provide a rather large spread for this parameter (Table S7) with none of the twisted-core models reproducing experimental values very well. However, it appears that the uncertainties obtained for $|\eta|$ in the ESEEM simulations are also considered larger than those for e^2qQ/h. For example, for the Mn^{III} site in two different dimanganese catalases (from *Lactobacillus plantarum* and *Thermus thermophilus*), the measured $|\eta|$ values differed significantly,[89] whereas the e^2qQ/h values agreed closely.

Carboxylate ^{13}C hyperfine tensors: Recently, Stull et al.[40] applied ^{13}C ENDOR to the S_2 state for PSII preparation in which either all the alanine carboxylate carbons or all the carbon atoms were ^{13}C-labelled for comparison with the bridging carboxylate in a dinuclear $Mn^{III}Mn^{IV}$ complex. They concluded that the D1 polypeptide terminus is bound to manganese. In the simulations of the ENDOR spectra, Stull et al. had to make a number of assumptions, which involved dipolar HFCs estimated by the point–dipole approximation from the different known X-ray structures. For both models evaluated here, D1-Ala344 is most likely coordinated as a bridging ligand between Mn_D and the calcium atom. However, in view of the uncertainties in the X-ray structure determinations due to radiation damage, this is so far a highly speculative assignment. To see to what extent the hyperfine couplings could be characteristic of the bonding mode, we compute here the ^{13}C HFC tensors for all carboxylate ligands present in the **SG2009^{-1}** and **YII-1^0** models.

Table 5 summarizes the computational results obtained for the lowest BS state of each model (as for ^{14}N HFCs, no scaling of the B3LYP HFCs was carried out here), in which the alanine is bonded to one manganese center (in the London X-ray structure, the alanine is suggested to be bonded only to calcium, an alternative disfavored in ref. [40]), and compares them with ENDOR data. For car-

Table 5. Comparison of computed ^{13}C HFC tensors for different carboxylato ligands with ENDOR data for ^{13}C-labelled PSII D1-Ala344 (in MHz).

	Position	Projection	a_{iso}(site)	A_{iso}	T_1	T_2	T_3	$\rho^{\alpha-\beta}$
SG2009^{-1}	Mn_D–Ca[a]		2.1	−2.1	−1.5	0.7	0.8	−0.005
$A\bar{B}C\bar{D}$	Mn_A–term.[b]		1.8	2.3	−1.3	−0.9	2.3	0.009
	Mn_C–term.[b]		3.1	5.3	−1.4	−1.1	2.5	0.005
	Mn_A–Mn_B	Mn A[c]	−0.1	−0.1	−2.9	0.5	2.3	
		Mn B[d]	0.1	−0.1	−2.2	0.4	1.8	
		weighted[e]		−0.1	2.5	0.5	2.1	−0.002
	Mn_B–Mn_D	Mn B[c]	1.9	−1.9	−1.5	0.2	1.3	
		Mn D[d]	1.9	−1.9	−1.5	0.2	1.3	
		weighted[e]		−1.9	−1.5	0.2	1.3	−0.002
	Mn_C–Mn_D	Mn C[c]	−1.4	−2.3	−2.8	−0.5	3.3	
		Mn D[d]	1.8	−1.8	−2.2	−0.4	2.6	
		weighted[e]		−2.1	−2.5	−0.4	3.0	−0.003
YII-1^0	MnD–Ca[a]		0.6	1.1	−1.0	−0.8	1.8	0.003
$A\bar{B}\bar{C}D$	Mn_A–term.[b]		1.8	2.4	−0.9	−0.8	1.7	0.003
	Mn_C–term.[b]		2.8	−2.8	−1.8	0.5	1.3	−0.003
	Mn_A–Mn_B	Mn A[c]	−0.1	−0.1	−2.2	−0.3	2.5	
		Mn B[d]	0.1	−0.1	−1.7	−0.3	2.0	
		weighted[e]		−0.1	−2.0	−0.3	2.3	−0.003
	Mn_B–Mn_D	Mn B[c]	−1.1	1.1	−2.2	−0.5	2.7	
		Mn D[d]	0.8	1.4	−2.8	−0.7	3.5	
		weighted[e]		1.2	−2.5	−0.6	3.1	−0.002
	Mn_C–Mn_D	Mn C[c]	−0.3	0.3	−2.2	−0.1	2.3	
		Mn D[d]	0.2	0.3	−2.8	−0.1	3.0	
		weighted[e]		0.3	−2.5	−0.1	2.6	−0.001
exp.	structure[f]							
	Loll			1.2	−2.2	0.8	1.4	
	Guskov			1.0	−2.0	−1.5	3.5	

[a] Results for carboxylate bridging Mn_D and Ca. [b] Results for terminal carboxylate. [c] HFC data for bridging carboxylate using spin-projection coefficient for the first center. [d] HFC data for bridging carboxylate using spin-projection coefficient for the second center. [e] HFC tensor for bridging carboxylate calculated by weighting the differently projected tensors with the corresponding Mn–^{13}C distances. [f] Simulations based on Q-band Mims ENDOR data.[40] The results are based on a weighted spin projection using distances from different X-ray structures by Loll et al.[9] and Guskov et al. (A. Guskov, J. Kern, A. Gabdulkhakov, M. Broser, A. Zouni, W. Saenger, *Nat. Struct. Mol. Biol.* **2009**, *16*, 334–342 (see text).[40]

boxylates that symmetrically bridge two manganese sites, we have spin-projected the intrinsic HFC tensors first for either of the two sites [according to the spin-projection coefficients of Eq. (15)] and then averaged the two resulting coupled tensors. A distance-weighted averaging gave identical results due to the essentially symmetrical bridge (no spectral simulations along these lines are available so far). For terminal or Mn–Ca bridging carboxylates, spin-projection factors were taken only for the directly bonded manganese site in the given BS state.

The data in Table 5 indicate that it is difficult to give a unique assignment for two reasons: 1) Several bonding situations provide rather similar projected tensors and 2) the uncertainties and approximations involved in the ENDOR simulations are too large. We may, however, exclude a few possibilities. In particular, it appears 1) that a terminal carboxylate on Mn_C without compensation of its negative charge gives isotropic HFCs that are much too large. This holds particularly for **SG2009^{-1}** in which Mn_C is the Mn^{III} site. 2) A carboxylate bridging the antiferromagnetically coupled Mn^{IV}–Mn^{IV} pair, Mn_A–Mn_B, exhibits a vanishing isotropic HFC for both models. This also seems to be in disagreement with the ENDOR spectra.[40]

The apparently best overall agreement with the simulation results would be for an Mn_B–Mn_D bridging site in **YII-1^{0}**. Carboxylates bridging Mn_B and Mn_D or Mn_C and Mn_D in **SG2009^{-1}** give larger A_{iso} values than the ENDOR simulations, but this may be within the combined uncertainties of the computations and simulations.[40] Symmetrically bridging carboxylates generally provide larger HFC anisotropies and larger rhombicities than terminal or Mn_D–Ca bridging ligands, but this may also be outside the current accuracy of the measurements.

Conclusion

The computation of EPR parameters for different structural models of the OEC and their comparison with experimental data provides the intriguing possibility of reducing the number and type of acceptable structural models. Owing to the electronic complexity of the spin-coupled tetranuclear cluster, BS-DFT calculations followed by spin projection are currently the only way to access the parameters of the EPR, ENDOR, or ESEEM spectra of the OEC in a meaningful way by quantum-chemical methods. Close analysis of a recently suggested procedure for obtaining the necessary spin-projection coefficients by a numerical fit of the HDvV Hamiltonian indicates that the currently available accuracy of BS-DFT is not generally sufficient to arrive at very reliable coefficients. Together with the possible importance of the currently neglected ZFS contributions to the spin-projection matrices, this limits the accuracy of computed hyperfine coupling tensors. Alternative spin-projection coefficients based on the consideration of some inter-relations between the Heisenberg exchange coupling constants provide a simplified and more easily applicable projection scheme with little loss of accuracy. We also found that the exchange coupling constants computed here overall exhibit far smaller values than assumed before from the knowledge of dinuclear $Mn^{III}Mn^{IV}$ complexes. This is an important observation, as substantial structural conclusions have frequently been based on the assumed, much larger antiferromagnetic couplings.

Computed ^{55}Mn HFCs for a recently refined, energetically feasible, and mechanistically based model cluster, **SG2009^{-1}**, agree excellently with the results of EPR and ENDOR spectra simulations for the S_2 state, but other models provide almost as good agreement within the expected accuracy of the computational scheme. Current work concentrates on improved projection schemes, including zero-field splitting effects for improved accuracy and access to the HFC anisotropies. An interesting observation of this work is that, due to the relatively small intrinsic HFC for the five-coordinate Mn^{III} site, the computed projected value is not guaranteed to be the largest of the four manganese HFCs. The latter assumption seems to be intrinsic to previous interpretations of the spectral simulations, a point that may have to be reconsidered.

Most notably, the present extension to ligand magnetic resonance parameters provides further insights: Although the computed isotropic ^{14}N HFCs for a coordinated histidine tend to underestimate experimental values somewhat, the ^{14}N HFC anisotropies appear particularly informative. **SG2009^{-1}** is singular among the more widely considered models in having the histidine residue D1-His332 bound to the unique Mn^{III} center of the S_2 state. The computed ^{14}N HFC anisotropy for this model is more than a factor of two larger than for all other models and agrees closely with the simulation of the ESEEM spectra. This is partly due to an intrinsically larger anisotropy and partly due to the larger spin-projection coefficient for the Mn^{III} site, and it agrees with the interpretation of the experiments. Even with the limitations of the spin-projection procedures in mind, this provides support for the **SG2009^{-1}** model and for the considerations attached to it regarding the reaction mechanism of water oxidation by the OEC. This indicates furthermore that hyperfine couplings of ligands bonded to the OEC may provide even more diagnostic probes than the ^{55}Mn HFCs. As a further example, ^{13}C HFCs have been computed for a variety of carboxylate carbon nuclei in the ligand framework of the models. The introduction and study of specifically isotope-labeled amino acids or substrate analogues into the OEC is currently a very active area of research. In combination with quantum-chemical calculations like those presented here, such experiments may provide substantial further insights into all S states of the OEC observable by magnetic resonance techniques.

Acknowledgements

This work has been supported by the Deutsche Forschungsgemeinschaft (KA 1187/9-2, KA 1187/12-1). We thank R. David Britt, Troy A. Stich,

Jamie A. Stull (UC Davis), and Robert Bittl (FU Berlin) for fruitful discussions. We acknowledge Christoph S. W. Fischer, Bartosz Zarzycki, and Michael Steinbauer for help with the construction of some of the initial model systems and Roman Reviakine and Peter Hrobarik for technical assistance. S.S. thanks the Fonds der Chemischen Industrie and the German Academic Exchange Service for scholarships.

[1] N. S. Lewis, D. G. Nocera, *Proc. Natl. Acad. Sci. USA* **2006**, *103*, 15729.
[2] B. Kok, B. Forbush, M. McGloin, *Photochem. Photobiol.* **1970**, *11*, 457.
[3] W. Junge, M. Haumann, R. Ahlbrink, A. Mulkidjanian, J. Clausen, *Philos. Trans. R. Soc. B* **2002**, *357*, 1407.
[4] J. Lavergne, W. Junge, *Photosynth. Res.* **1993**, *38*, 279.
[5] E. Schlodder, H. T. Witt, *J. Biol. Chem.* **1999**, *274*, 30387.
[6] H. Dau, M. Haumann, *Coord. Chem. Rev.* **2008**, *252*, 273.
[7] M. Haumann, P. Liebisch, C. Mueller, M. Barra, M. Grabolle, H. Dau, *Science* **2005**, *310*, 1019.
[8] H. Dau, M. Haumann, *Photosynth. Res.* **2007**, *92*, 327.
[9] B. Loll, J. Kern, W. Saenger, A. Zouni, J. Biesiadka, *Nature* **2005**, *438*, 1040.
[10] A. Zouni, H. T. Witt, J. Kern, P. Fromme, N. Krauss, W. Saenger, P. Orth, *Nature* **2001**, *409*, 739.
[11] K. N. Ferreira, T. M. Iverson, K. Maghlaoui, J. Barber, S. Iwata, *Science* **2004**, *303*, 1831.
[12] N. Kamiya, J.-R. Shen, *Proc. Natl. Acad. Sci. USA* **2003**, *100*, 98.
[13] J. Barber, *Inorg. Chem.* **2008**, *47*, 1700.
[14] J. Yano, V. K. Yachandra, *Inorg. Chem.* **2008**, *47*, 1711.
[15] T. Noguchi, *Coord. Chem. Rev.* **2008**, *252*, 336.
[16] Y. Taguchi, T. Noguchi, *Biochim. Biophys. Acta Bioenerg.* **2007**, *1767*, 535.
[17] J. P. Decker, *Manganese Redox Enzymes* /Ed, : V. L. Pecoraro), **1992**, VCH, Weinheim, p. 85.
[18] R. D. Britt, K. A. Campbell, J. M. Peloquin, M. L. Gilchrist, C. P. Aznar, M. M. Dicus, J. Robblee, J. Messinger, *Biochim. Biophys. Acta Bioenerg.* **2004**, *1655*, 158.
[19] A. Haddy, *Photosynth. Res.* **2007**, *92*, 357.
[20] J. Yano, J. Kern, K.-D. Irrgang, M. J. Latimer, U. Bergmann, P. Glatzel, Y. Pushkar, J. Biesiadka, B. Loll, K. Sauer, J. Messinger, A. Zouni, V. K. Yachandra, *Proc. Natl. Acad. Sci. USA* **2005**, *102*, 12047.
[21] J. Barber, J. W. Murray, *Coord. Chem. Rev.* **2008**, *252*, 233.
[22] H. Dau, P. Liebisch, M. Haumann, *Phys. Chem. Chem. Phys.* **2004**, *6*, 4781.
[23] M. Grabolle, M. Haumann, C. Mueller, P. Liebisch, H. Dau, *J. Biol. Chem.* **2005**, *281*, 4580.
[24] J. Yano, J. Kern, K. Sauer, M. J. Latimer, Y. Pushkar, J. Biesiadka, B. Loll, W. Saenger, J. Messinger, A. Zouni, V. K. Yachandra, *Science* **2006**, *314*, 821.
[25] H. Dau, A. Grundmeier, P. Loja, M. Haumann, *Philos. Trans. R. Soc. B* **2008**, *363*, 1237.
[26] G. C. Dismukes, Y. Siderer, *FEBS Lett.* **1980**, *121*, 78.
[27] G. C. Dismukes, Y. Siderer, *Proc. Natl. Acad. Sci. USA* **1981**, *78*, 274.
[28] J. L. Casey, K. Sauer, *Biochim. Biophys. Acta Bioenerg.* **1984**, *767*, 21.
[29] J. L. Zimmermann, A. W. Rutherford, *Biochim. Biophys. Acta Bioenerg.* **1984**, *767*, 160.
[30] J. M. Peloquin, K. A. Campbell, D. W. Randall, M. A. Evanchik, V. L. Pecoraro, W. H. Armstrong, R. D. Britt, *J. Am. Chem. Soc.* **2000**, *122*, 10926.
[31] L. V. Kulik, B. Epel, W. Lubitz, J. Messinger, *J. Am. Chem. Soc.* **2005**, *127*, 2392.
[32] M.-F. Charlot, A. Boussac, G. Blondin, *Biochim. Biophys. Acta Bioenerg.* **2005**, *1708*, 120.
[33] J. M. Peloquin, R. D. Britt, *Biochim. Biophys. Acta Bioenerg.* **2001**, *1503*, 96.
[34] L. V. Kulik, B. Epel, W. Lubitz, J. Messinger, *J. Am. Chem. Soc.* **2007**, *129*, 13421.
[35] D. W. Randall, B. E. Sturgeon, J. A. Ball, G. A. Lorigan, M. K. Chan, M. P. Klein, W. H. Armstrong, R. D. Britt, *J. Am. Chem. Soc.* **1995**, *117*, 11780.
[36] D. W. Randall, M. K. Chan, W. H. Armstrong, R. D. Britt, *Mol. Phys.* **1998**, *95*, 1283.
[37] C. Teutloff, K.-O. Schaefer, S. Sinnecker, V. Barynin, R. Bittl, K. Wieghardt, F. Lendzian, W. Lubitz, *Magn. Reson. Chem.* **2005**, *43*, S51.
[38] G. J. Yeagle, M. L. Gilchrist, Jr., L. M. Walker, R. J. Debus, R. D. Britt, *Philos. Trans. R. Soc. B* **2008**, *363*, 1157.
[39] G. J. Yeagle, M. L. Gilchrist, R. M. McCarrick, R. D. Britt, *Inorg. Chem.* **2008**, *47*, 1803.
[40] J. A. Stull, T. A. Stich, R. J. Service, R. J. Debus, S. K. Mandal, W. H. Armstrong, R. D. Britt, *J. Am. Chem. Soc.* **2009**, *131*, 446.
[41] L. Noodleman, *Coord. Chem. Rev.* **1995**, *144*, 199.
[42] L. Noodleman, *J. Chem. Phys.* **1981**, *74*, 5737.
[43] S. Sinnecker, F. Neese, L. Noodleman, W. Lubitz, *J. Am. Chem. Soc.* **2004**, *126*, 2613.
[44] S. Sinnecker, F. Neese, W. Lubitz, *J. Biol. Inorg. Chem.* **2005**, *10*, 231.
[45] D. A. Pantazis, M. Orio, T. Petrenko, S. Zein, W. Lubitz, J. Messinger, F. Neese, *Phys. Chem. Chem. Phys.* **2009**, *11*, 6788.
[46] P. E. M. Siegbahn, *J. Am. Chem. Soc.* **2009**, *131*, 18238.
[47] P. E. M. Siegbahn, *Acc. Chem. Res.* **2009**, *42*, 1871.
[48] P. E. M. Siegbahn, *Inorg. Chem.* **2008**, *47*, 1779.
[49] P. E. M. Siegbahn, *Philos. Trans. R. Soc. B* **2008**, *363*, 1221.
[50] P. E. M. Siegbahn, *Chem. Eur. J.* **2008**, *14*, 8290.
[51] A. Bencini, D. Gatteschi, *EPR of Exchange Coupled Systems*, Springer, Berlin, **1990**.
[52] A. Abragam, B. Bleaney, *Electron Paramagnetic Resonance of Transition Ions*, Clarendon Press, Oxford, **1970**.
[53] M. Kaupp, M. Bühl, V. G. Malkin, *Calculation of NMR and EPR Parameters: Theory and Applications*, Wiley-VCH, Weinheim, **2004**.
[54] J. E. Harriman, *Theoretical Foundations of Electron Spin Resonance*, Academic Press, New York, **1978**.
[55] N. M. Atherton, *Principles of Electron Spin Resonance*, Prentice Hall, New York, **1993**.
[56] F. E. Mabbs, D. Collison, *Electron Paramagnetic Resonance of d Transition Metal Compounds*, Elsevier, Amsterdam, **1992**.
[57] B. R. McGarvey, *Transition Met. Chem.* **1966**, *3*, 89.
[58] A. V. Arbuznikov, J. Vaara, M. Kaupp, *J. Chem. Phys.* **2004**, *120*, 2127.
[59] C. Remenyi, R. Reviakine, A. V. Arbuznikov, J. Vaara, M. Kaupp, *J. Phys. Chem. A* **2004**, *108*, 5026.
[60] F. Neese, *J. Chem. Phys.* **2003**, *118*, 3939.
[61] G. Blondin, J. J. Girerd, *Chem. Rev.* **1990**, *90*, 1359.
[62] P. Bertrand, B. Guigliarelli, C. More, *New J. Chem.* **1991**, *15*, 445.
[63] R. H. Sands, W. R. Dunham, *Q. Rev. Biophys.* **1975**, *8*, 443.
[64] M. Zheng, S. V. Khangulov, G. C. Dismukes, V. V. Barynin, *Inorg. Chem.* **1994**, *33*, 382.
[65] S. Schinzel, M. Kaupp, *Can. J. Chem.* **2009**, *87*, 1521.
[66] D. A. Pantazis, M. Orio, T. Petrenko, S. Zein, E. Bill, W. Lubitz, J. Messinger, F. Neese, *Chem. Eur. J.* **2009**, *15*, 5108.
[67] M. Shoji, K. Koizumi, Y. Kitagawa, T. Kawakami, S. Yamanaka, M. Okumura, K. Yamaguchi, *Chem. Phys. Lett.* **2006**, *432*, 343.
[68] S. Zein, C. Duboc, W. Lubitz, F. Neese, *Inorg. Chem.* **2008**, *47*, 134.
[69] S. Zein, L. V. Kulik, J. Yano, J. Kern, Y. Pushkar, A. Zouni, V. K. Yachandra, W. Lubitz, F. Neese, J. Messinger, *Philos. Trans. R. Soc. B* **2008**, *363*, 1167.
[70] R. Ahlrichs, M. Bär, M. Häser, H. Horn, C. Kölmel, *Chem. Phys. Lett.* **1989**, *162*, 165.
[71] A. D. Becke, *J. Chem. Phys.* **1993**, *98*, 5648.
[72] P. J. Stephens, F. J. Devlin, C. F. Chabalowski, M. J. Frisch, *J. Phys. Chem.* **1994**, *98*, 11623.
[73] A. Schäfer, H. Horn, R. Ahlrichs, *J. Chem. Phys.* **1992**, *97*, 2571.
[74] M. Munzarová, M. Kaupp, *J. Phys. Chem. A* **1999**, *103*, 9966.

[75] M. Munzarová, P. Kubácek, M. Kaupp, *J. Am. Chem. Soc.* **2000**, *122*, 11900.
[76] W. Kutzelnigg, U. Fleischer, M. Schindler, *NMR Basis Principles and Progress, Vol. 23* (Eds.: P. Diehl, E. Fluck, H. Günther, R. Kosfeld, J. Seelig), Springer, Berlin, **1990**, p. 1.
[77] S. Huzinaga, Ph.D. thesis **1971**, University of Alberta (Edmonton).
[78] S. Schinzel, R. Müller, M. Kaupp, *Theor. Chem. Acc.* **2008**, *120*, 437.
[79] V. N. Staroverov, G. E. Scuseria, J. Tao, J. P. Perdew, *J. Chem. Phys.* **2003**, *119*, 12129.
[80] MAG-Respect, Version 2.1, V. G. Malkin, O. L. Malkina, R. Reviakine, A. V. Arbouznikov, M. Kaupp, B. Schimmelpfennig, I. Malkin, T. Helgaker, K. Ruud, **2007**.
[81] B. A. Hess, C. M. Marian, U. Wahlgren, O. Gropen, *Chem. Phys. Lett.* **1996**, *251*, 365.
[82] B. Schimmelpfennig, Ph.D. thesis **1996**, Stockholms Universitet (Sweden).
[83] S. Portmann, H. P. Luthi, *Chimia* **2000**, *54*, 766.
[84] G. A. Lorigan, R. D. Britt, *Biochemistry* **1994**, *33*, 12072.
[85] R. J. Pace, P. Smith, R. Bramley, D. Stehlik, *Biochim. Biophys. Acta* **1991**, *1058*, 161.
[86] M. Orio, D. A. Pantazis, T. Petrenko, F. Neese, *Inorg. Chem.* **2009**, *48*, 7251.
[87] C. Teutloff, S. Pudollek, S. Keßen, M. Broser, A. Zouni, R. Bittl, *Phys. Chem. Chem. Phys.* **2009**, *11*, 6715.
[88] C. Remenyi, R. Reviakine, M. Kaupp, *J. Phys. Chem. B* **2007**, *111*, 8290.
[89] T. A. Stich, J. W. Whittaker, R. D. Britt, *J. Phys. Chem. B* **2010**, DOI: 0.1021/jp908064y.
[90] K. O. Schäfer, R. Bittl, F. Lendzian, V. Barynin, T. Weyhermueller, K. Wieghardt, W. Lubitz, *J. Phys. Chem. B* **2003**, *107*, 1242.
[91] C. I. H. Ashby, C. P. Cheng, E. N. Duesler, T. L. Brown, *J. Am. Chem. Soc.* **1978**, *100*, 6063.

Received: March 5, 2010
Published online: July 19, 2010

